RSC Advances

PAPER

View Article Online
View Journal | View Issue

Check for updates

Cite this: *RSC Adv.*, 2024, **14**, 6762

# *Ab initio* investigations of the structure-stability, mechanical, electronic, thermodynamic and optical properties of $Ti_2FeAs$ Heusler alloy

Anjali Kumari,[a] Abhishek Kumar Mishra,†[a] Ramesh Sharma,[b] Samah Al-Qaisi,[c] A. J. A. Moayad,*[d] Ali S. Alshomrany,[e] N. Sfina,[f] Sajad Ahmed Dar[g] and Vipul Srivastava *[h]

In this study, we employed density functional theory coupled with the full-potential linearized augmented plane-wave method (FP-LAPW) to investigate the structural, electronic, and magnetic properties of the $Ti_2FeAs$ alloy adopting the $Hg_2CuTi$-type structure. Our findings demonstrate that all the examined structures exhibit ferromagnetic (FM) behaviour. By conducting electronic band structure calculations, we observed an energy gap of 0.739 eV for $Ti_2FeAs$ in the spin-down state and metallic intersections at the Fermi level in the spin-up state. These results suggest the half-metallic (HM) nature of $Ti_2FeAs$, where the Ti-d and Fe-d electronic states play a significant role near the Fermi level. Additionally, the obtained total magnetic moments are consistent with the Slater–Pauling rule ($M_{tot} = Z_{tot} - 18$), indicating 100% spin polarization for these compounds. To explore their optical properties, we employed the dielectric function to compute various optical parameters, including absorption spectra, energy-loss spectra, refractive index, reflectivity, and conductivity. Furthermore, various thermodynamic parameters were evaluated at different temperatures and pressures. The results obtained from the elastic parameters reveal the anisotropic and ductile nature of the $Ti_2FeAs$ compound. These findings suggest that $Ti_2FeAs$ has potential applications in temperature-tolerant devices and optoelectronic devices as a UV absorber.

Received 24th October 2023
Accepted 7th February 2024

DOI: 10.1039/d3ra07249e

rsc.li/rsc-advances

Open Access Article. Published on 23 February 2024. Downloaded on 2/5/2026 12:43:03 AM.
This article is licensed under a Creative Commons Attribution-NonCommercial 3.0 Unported Licence.

## 1. Introduction

Spintronics, a rapidly growing field in electronics, utilizes the intrinsic angular momentum or spin of electrons to process information. The discovery of giant magnetoresistance (GMR) in 1988 paved the way for significant advancements in nanomagnetism and spintronics.[1–5] In this field, materials known as spintronic materials, such as ferromagnetic metals, magnetic semiconductors (with or without doping), and a special class called "half metals," play a crucial role. Among them, half-metallic ferromagnets (HMFs) are desirable due to their unique characteristic of 100% spin polarization at the Fermi level. This means that they conduct electricity only with one spin orientation, while acting as insulators for the other, thereby exhibiting both metallic and semiconducting behaviours.[6] HMFs serve as efficient spin filters, enabling high spin-polarized currents and playing a vital role in various spin-dependent phenomena such as tunnelling magnetoresistance (TMR) and spin injection into semiconductors.[7–9] These materials are identified through spin-dependent band-structure computations and hold potential importance as sources and analysers of polarized electrons in spintronic devices. De Groot *et al.* reported the first prediction of half-metallic behaviour while studying NiMnSn using *ab initio* calculations.[10] The other materials investigated in this field include double perovskites, Heusler alloys, rare-earth nitrides, zinc blende transition metal pnictides, and chalcogenides.[11–17] Specifically, Heusler alloys show relatively high Curie temperatures, showing an advantage over other half-metallic systems.[18–21] Thus, they have been explored for application as spin filters, tunnel junctions, and GMR devices.[22,23] Half-Heusler alloys such as NiMnSb have attracted significant interest and full-Heusler alloys have also been extensively studied due to their diverse magnetic

[a]*Department of Physics, Applied Science Cluster, University of Petroleum and Energy Studies, Bidholi via Premnagar, Dehradun, Uttrakhand 248007, India*
[b]*Department of Applied Science, Feroze Gandhi Institute of Engineering and Technology, Raebareli, 229001, Uttar Pradesh, India*
[c]*Palestinian Ministry of Education and Higher Education, Nablus, Palestine*
[d]*Department of Material Science, Malawi University of Science and Technology, Limbe, Malawi. E-mail: mailme_moya123@gmail.com*
[e]*Department of Physics, College of Sciences, Umm Al-Qura University, Al Taif HWY, Mecca 24381, Saudi Arabia*
[f]*College of Sciences and Arts in Mahayel Asir, Department of Physics, King Khalid University, Abha, Saudi Arabia*
[g]*Department of Physics, Govt. Motilal Vigyan Mahavidyalaya College, Bhopal, Madhya Pradesh, India*
[h]*Department of Physics, School of Chemical Engineering & Physical Sciences, Lovely Professional University, Delhi-Jalandhar Highway, Phagwara-144411, Punjab, India. E-mail: vipsri27@gmail.com*
† Computational Materials and Photonics, FB 16, University of Kassel, Wilhelmshöher Allee 71, 34121, Germany.


© 2024 The Author(s). Published by the Royal Society of Chemistry

Open Access Article. Published on 23 February 2024. Downloaded on 2/5/2026 12:43:03 AM.
This article is licensed under a Creative Commons Attribution-NonCommercial 3.0 Unported Licence.

phenomena.[24–28] The transition from a ferromagnetic phase to an antiferromagnetic phase by modifying the carrier concentration has become a prominent area of study in full-Heusler alloys.[29] Full-Heusler alloys are the $X_2YZ$ type, where X and Y represent transition metals or lanthanides and Z represents an atom from the main group (III or IV) of the periodic table.[30] These alloys crystallize in an $L2_1$ structure, consisting of four FCC sublattices. The full-Heusler alloys containing cobalt were first synthesized, and compounds such as $Co_2MnZ$ (Z = Si and Ge) were proposed to be half-ferromagnets.[31–34] The complex nature of the full-Heusler alloys, which have two X atoms, adds to their intrigue for magneto-electronic applications due to their semiconductor-like structure and high Curie temperature.[35–38]

For the development of high-performance spintronic devices, three crucial requirements need to be satisfied for HMFs, as follows: (1) a high Curie temperature for room-temperature applications, (2) a large bulk magneto-crystalline anisotropy energy to counteract unwanted spin switching caused by thermal fluctuations and (3) a wide half-metallic gap to effectively prevent spin-flip transitions due to thermal excitation.[39] Therefore, understanding the stability and Curie temperature of HM materials is essential for their development and utilization in spintronic devices. Our present study on DFT calculations for $Ti_2FeAs$ was motivated by considering a literature review on the marvellous applications of similar Heusler alloys in the field of technology. The integration of spin-based electronics is expected to revolutionize the fields of information technology, memory technology, and telecommunications, offering numerous advantages.

This paper is organized as follows: Section 2 describes the methods and essentials of the code to calculate physical properties. Section 3 presents the potential results and discussion on the various physical properties of the $Ti_2FeAs$ compound. In Section 4, the results are concluded with the scope of this study.

## 2. Computational details

The calculations for determining the electronic structure were performed by the implementation of the FP-LAPW method[40–42] based on density functional theory (DFT)[43,44] *via* the WIEN2k code.[45] To account for the exchange–correlation effects, the generalized gradient approximation (PBE-GGA) by Perdew, Burke, and Ernzerhof[46] as well as the local spin-density approximation (LSDA) by Perdew and Wang[47] was employed. Furthermore, for the accurate determination of electronic properties, the modified Becke–Johnson (mBJ) exchange potential developed by Trans and Blaha (TB)[48] was utilized. The TB-mBJ(GGA) approach was employed to address the underestimation of the band gap using GGA and increase the accuracy of other related properties. The real space was partitioned into two areas using the FP-LAPW approach, as follows: (1) incorporating non-overlapping spheres escorted by a muffin-tin radius ($R_{MT}$) around the atomic sites and (2) corresponding to the interstitial region. Inside the first domain, the wave functions, electron density, and potential were enlarged using spherical harmonic combinations up to $l_{max} = 10$, while in domain 2, a Fourier series or plane waves up to a cutoff radius of $R_{MT} \times K_{max} = 8$ were employed. The chosen muffin-tin radii for Ti, Fe, and As were 2.20 a.u, 2.00 a.u, and 2.00 a.u, respectively, to ensure non-overlapping of the muffin-tin spheres. The specific values of $R_{MT}$ utilized in this study are provided in Table 1. The maximum vector responsible for Fourier expansion of the density ($G_{max}$) was set to a magnitude of 14. For sampling the first Brillouin zone, a total of 1000 special $k$ points was selected. The power-cut zone, which separated the valence and core region, was set to −6.0 Ry. Within 0.1 mRy, when the total energy stabilised, the self-consistent computations were regarded as having converged. In our calculations, the electronic configuration of Ti [Ar]: $3d^2$, $4s^2$; Fe [Ar]: $3d^6$, $4s^2$; and As [Ar]: $3d^{10}$, $4s^2$, $4p^3$ were treated as valence states.

## 3. Results and discussion

### 3.1 Structure stability

As stated in the Introduction, Heusler alloys have the chemical formula of $X_2YZ$, where X and Y represent transition elements and Z denotes a main group atom. The ordered cubic alloy $X_2YZ$ can adopt two distinct structures, *i.e.*, the "regular" type, exemplified by $Cu_2MnAl$ with the $L2_1$ prototype structure (space group $Fm\bar{3}m$ no. 225) and the "inverse" Heusler type, such as $Hg_2CuTi$ (XA), which follows the $Li_2AgSb$ structure (space group $F\bar{4}3m$ no. 216). In, the present study, the structural, electronic, and magnetic properties of the $Ti_2FeAs$ ($Hg_2CuTi$, prototype XA) structure, as shown in Fig. 1, with the space group $F\bar{4}3m$ no. 216 were calculated. The LSDA and PBE-GGA methods were used to study the structural properties. To examine the magnetic stability of the $Ti_2FeAs$ compound, we initiated the calculation

Table 1 The calculated lattice parameter $a_0$, volume $V_0$, bulk modulus $B_0$, derivative of the bulk $B'_0$ equilibrium total energy $E_0$, cohesive energy ($E_{Coh}$) and formation energy ($\Delta H$)$_f$ for $Ti_2FeAs$ for phases in the NM and FM states using the GGA-PBE and LSDA approximation

| $Ti_2FeAs$ | Phases | $a_0$ (Å) | $V_0$ (a.u$^3$) | $B'_0$ | $E_0$ (Ry) | $E_{Coh}$ (eV per atom) | ($\Delta H$)$_f$ (eV per atom) | $\Delta E$ (Ry) = $E_{NM} - E_{FM}$ |
|---|---|---|---|---|---|---|---|---|
| PBE-GGA | FM | 6.07 | 379.04 | 6.36 | −10483.105 | 5.37 | −0.71 | 0.016049 |
| | NM | 6.06 | 376.26 | 7.80 | −10483.089 | | | |
| LSDA | FM | 6.07 | 378.54 | 6.11 | −10483.103 | 66.99 | −0.64 | 17.71 |
| | NM | 5.93 | 352.13 | 3.15 | −10465.391 | | | |
| | | Ref. 54 | | | | | | |

Open Access Article. Published on 23 February 2024. Downloaded on 2/5/2026 12:43:03 AM.
This article is licensed under a Creative Commons Attribution-NonCommercial 3.0 Unported Licence.

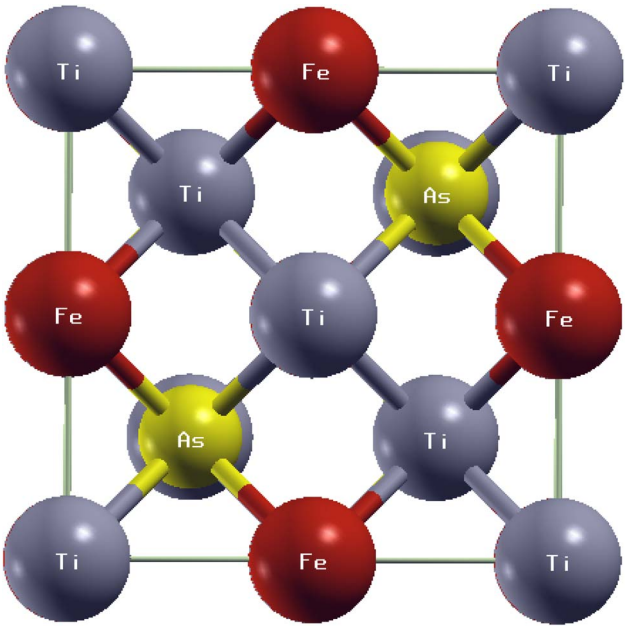


Fig. 1 $Ti_2FeAs$ in the *F*43*m* space group regular-type ($Hg_2CuTi$, prototype XA) structure.

by determining the energy difference ($\Delta E = E_{NM} - E_{FM}$) between the nonmagnetic (NM) and ferromagnetic (FM) configurations. In this case, we employed the Birch–Murnaghan equation of state,[49] which characterizes the energy variation with respect to volume (as depicted in Fig. 2). The lattice parameter utilized in our calculations is the predicted value obtained from earlier works.[50,51] The obtained equilibrium lattice constants ($a_0$), bulk modulus ($B_0$), pressure derivative ($B'_0$), and minimum total energies ($E$) for both the FM and NM configurations, together with other relevant theoretical data[51,52] are presented in Table 1. The results confirmed that the ferromagnetic configuration is stable for LSDA and PBE-GGA (Table 1) with the same energy. Our findings indicate an energy difference ($\Delta E$) of 0.01604 eV between the FM and NM states, suggesting the increased stability of the FM configuration of $Ti_2FeAs$. It is worth noting that available literature does not contain any confirmed theoretical or experimental information about the structural characteristics of $Ti_2FeAs$, thus making our results a prediction for this compound.

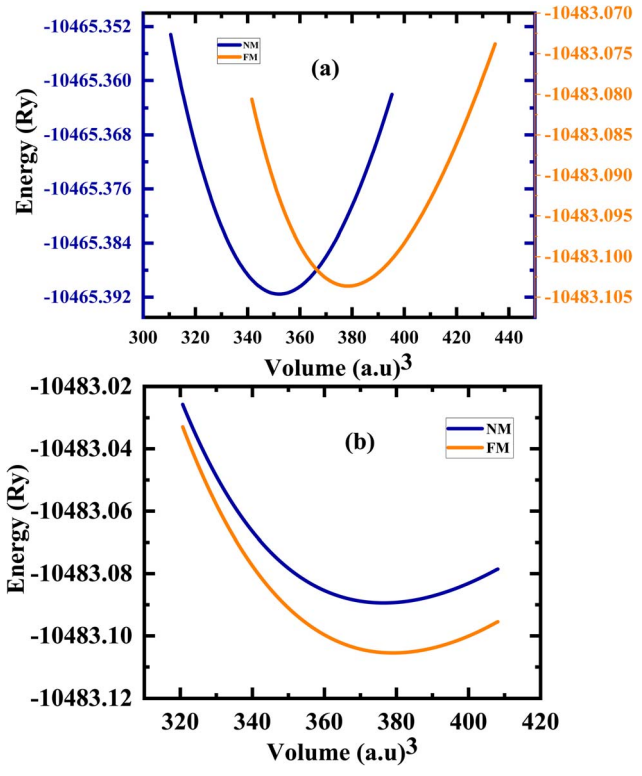


Fig. 2 Curve between energy (Ry) and volume of (a) LDA and (b) PBE-GGA for non-magnetic and ferromagnetic properties.

The assessment of stability can be approached from various perspectives, including physical, chemical, and mechanical aspects. One method to evaluate physical stability is through the calculation of cohesive energy, which quantifies the binding force between the atoms in a solid. The cohesive energy can be computed using the following relation:[53]

$$E_{Coh} = 2E^{Ti}_{atom} + E^{Fe}_{atom} + E^{As}_{atom} - E^{Ti_2FeAs}_{total} \quad (1)$$

where $E_{Coh}$ is the total energy of the compound at equilibrium and $E^{Ti}$ and $E^{Fe}$ and $E^{As}$ are the total energies of each atom. The physical stability is ensured by the calculated positive value of the cohesive energy (Table 1).

In addition, the formation energy, which determines the chemical stability of a compound, is calculated as follows:[54]

$$(\Delta H)_f = E_{Ti_2FeAs} - 2E_{Ti} - E_{Fe} - E_{As} \quad (2)$$

where $E_{Ti_2FeAs}$, $E_{Ti}$, $E_{Fe}$, and $E_{As}$ are the total energies of $Ti_2FeAs$ calculated at equilibrium. The calculated low value of formation energy (Table 1) ensures the chemical stability and confirms that the compound can be fabricated experimentally.

### 3.2 Mechanical properties

The elastic properties were calculated using the IRelast[55] method developed by J. Morteza as implemented in WIEN2k. Moreover, the mechanical stability was determined by calculating the elastic constants, which are only three for a cubic crystal, *i.e.*, $C_{11}$, $C_{12}$, and $C_{44}$, and the mechanical stability of the material cannot be ensured unless[56]

$$B = \frac{C_{11} + 2C_{12}}{3} > 0, \quad (3)$$

$$C_{11} - C_{12} > 0, \quad (4)$$

$$C_{44} > 0, \quad (5)$$

The elastic properties provide insightful information about the bonding nature between adjacent atomic planes. The elastic constants are utilized to evaluate the mechanical stability of the deformation of a crystal, given that they represent the coefficients that relate applied stress to strain. These constants


© 2024 The Author(s). Published by the Royal Society of Chemistry

Open Access Article. Published on 23 February 2024. Downloaded on 2/5/2026 12:43:03 AM. This article is licensed under a Creative Commons Attribution-NonCommercial 3.0 Unported Licence.

Table 2 Calculated values of elastic constant ($C_{ij}$), bulk modulus ($B$), shear modulus ($G$), Young's modulus ($E$), Poisson's ratio ($\sigma$), Pugh ratio ($B/G$), Frantsevich ratio ($G/B$), shear anisotropy factor ($A$), Cauchy pressure $C^P$, sound velocities (m s$^{-1}$), and Debye temperature $\theta_D$ (K) of $Ti_2FeAs$ at $P = 0$ GPa and $T = 0$ K

| Material property | Calculated value |
|---|---|
| Elastic constant $C_{11}$ (GPa) | 126.54 |
| Elastic constant $C_{12}$ (GPa) | 69.04 |
| Elastic constant $C_{44}$ (GPa) | 15.08 |
| Bulk modulus, $B$ (GPa) | 88.21 (ref. 55) |
| Shear modulus, $G$ (GPa) | 20.55 |
| Young's modulus, $E$ (GPa) | 57.21 |
| Poisson ratio, $\sigma$ (GPa) | 0.39 |
| Vickers hardness | 1.49 |
| Pugh ratio, $B/G$ | 4.29 |
| Frantsevich ratio, $G/B$ | 0.23 |
| Shear anisotropy factor, $A$ (GPa) | 0.52 |
| Cauchy pressure $C^P$ (GPa) | 53.96 |
| Transverse sound velocity (m s$^{-1}$) | 1738 |
| Longitudinal sound velocity (m s$^{-1}$) | 4200 |
| Average sound velocity (m s$^{-1}$) | 1967 |
| Temperature $\theta_D$ (K) | 192 |
| Melting temperature $T_{melt}$ (K) | 1762.3 |

describe the response, strength, and mechanical stability of a material under compression. In the case of a cubic crystal, mechanical stability is achieved when specific conditions are satisfied for the elastic constants ($C_{11}$, $C_{12}$ and $C_{44}$). These conditions include $C_{11} + 2C_{12} > 0$, $C_{11} > 0$, $C_{44} > 0$, $C_{11} - C_{12} > 0$, and $C_{12} < B < C_{11}$.[56]

Table 2 presents the computed elastic constants $C_{ij}$ ($i,j = 1,2$), different elastic moduli, Poisson ratio, Vickers hardness, Pugh ratio, Frantsevich ratio, anisotropy factor, Cauchy pressure, different velocities, Debye temperature and melting temperature of $Ti_2FeAs$. It can be concluded from Table 2 that the studied compound is mechanically stable given that all the elastic constants are positive and fulfil the stability conditions for the crystal lattice. $C_{11}$ and $C_{12}$ describe the response of the crystal to unidirectional compression, while $C_{44}$ is proportional to the shear modulus and indicates shear deformation. The value of $C_{11}$ is 88% higher than that of $C_{44}$, indicating greater resistance to compression compared to shear deformation. Table 2 demonstrates that the calculated bulk modulus at zero pressure, which was derived from the elastic constants, is 1.3% higher than that obtained through total energy optimization. Our findings highlight the significance of the $C_{11}$ constant over the other constants, emphasizing its importance in resisting length changes in this compound.

The Hill approximation can be used to derive modulus $B$, shear modulus $G$, Young's modulus $E$, and Poisson ratio $\sigma$ from the elastic constants. This approximation is based on the principles of the Reuss and Voigt approaches.[57,58]

With $B = B_H = B_V = B_R$ and $B = \frac{C_{11} + 2C_{12}}{3}$ (Hill's bulk modulus) and

$$G = \frac{1}{2}(G_V + G_R) = G_H(\text{Hill's shear}), \quad (6)$$

where Voigt's shear modulus

$$G_V = \frac{1}{5}(C_{11} - C_{12} + 3C_{44}) \quad (7)$$

Reuss's shear modulus

$$G_R = \frac{5(C_{11} - C_{12})C_{44}}{3(C_{11} - C_{12}) + 4C_{44}} \quad (8)$$

The calculated results are presented in Table 2. The value of $E$ and $\sigma$ are determined by the following relation:

$$B = \frac{E}{3(1 - 2\sigma)} \quad (9)$$

This relation determines the resistance of a material to volume changes upon the application of pressure with the help of the bulk modulus.[59]

In cubic materials, second-order elastic constants are used to estimate the shear modulus ($G$), which quantifies the resistance of a material to plastic deformation. Alternatively, $E$ is an essential parameter that represents the ratio of tensile stress to tensile strain. It provides a measure of the stiffness of a solid, where a higher Young's modulus indicates greater stiffness. Based on the values presented in Table 2, it can be inferred that the $Ti_2FeAs$ compound exhibits high rigidity due to its elevated Young's modulus. According to Frantsevich *et al.*,[61] metals having $\sigma$ above 1.75 are considered ductile, while those with $\sigma$ below 1.75 are deemed brittle. Therefore, the $Ti_2FeAs$ compound can be classified as ductile. However, due to the lack of available data for comparison, a direct assessment of our elastic constants, bulk modulus, and shear modulus results was not possible.

The computed elastic constants were also utilized to calculate the anisotropy parameter ($A$) using the following equation:

$$A = \frac{2C_{44}}{C_{11} - C_{12}} \quad (10)$$

This parameter provides crucial information about the stability of a structure and is closely associated with the potential development of micro-cracks in materials. Our results indicate significant anisotropy in the elastic properties of the compound. A value of $A$ of less than 1 suggests that the rigidity of the material is along the cube axis, while a value greater than 1 indicates greater rigidity along the diagonals of the body. According to our findings, the calculated value of $A$ is 0.52, indicating that the material is most rigid along the cube axis of the considered structure.

According to Pugh's criterion,[60] the $B/G$ ratio (bulk modulus to shear modulus ratio) defines the brittleness and ductility of a material. The material is regarded as brittle if its $B/G$ value is less than 1.75, whereas ductile if the $B/G$ value is more than or equal to 1.75. In the case of the considered present material *i.e.*, $Ti_2FeAs$, its value was calculated to be 4.29. This value serves as an indicator of the ductility of the material, and considering that it is larger than 1.75, it confirms its ductile nature. Further, Poisson's ratio ($\sigma$) can also be defined as the ratio of transverse contraction

Open Access Article. Published on 23 February 2024. Downloaded on 2/5/2026 12:43:03 AM. This article is licensed under a Creative Commons Attribution-NonCommercial 3.0 Unported Licence.

to longitudinal extension in the direction of elastic stress. For most metals, the lower limit of $\sigma$ is approximately 0.25.

The Debye temperature was determined from the average sound velocity, as indicated in eqn (11).

$$\theta_D = \frac{h}{k}\left[\frac{3n}{4\pi}\left(\frac{N_A\rho}{M}\right)\right]^{1/3} v_m \quad (11)$$

where $h$ denotes Planck's constant, $k$ refers to Boltzmann's constant, $N_A$ represents Avogadro's number, $n$ signifies the number of atoms per molecule or formula unit, $M$ denotes the molar mass, $\rho$ represents the density of the unit cell, and $v_m$ represents the average sound velocity. Eqn (12) further relates the average sound velocity to the compressional ($l$) and shear ($s$) sound velocity, as follows:

$$v_m = \left[\frac{1}{3}\left(\frac{2}{{v_t}^3} + \frac{1}{{v_l}^3}\right)\right]^{-1/3} \quad (12)$$

where $v_l$ and $v_t$ are the longitudinal and transverse sound velocities obtained by using the isotropic shear modulus $G$, the bulk modulus $B$ and the density $g$ from Navier's equation:

$$v_l = \left(\frac{3B+4G}{3g}\right)^{1/2} \text{ and } v_t = \left(\frac{G}{g}\right)^{1/2}$$

The Debye temperature ($\theta_D$), along with the compressional and shear wave velocities, was calculated and presented in Table 2. The Debye temperature is a crucial parameter that is strongly correlated with the melting point and specific heats of solids. Notably, our study provides the first reported value of $\theta_D$ for $Ti_2FeAs$. A high Debye temperature indicates a rigid crystal structure and is associated with an elevated melting point. Given that the Debye temperature represents the energy required to activate all phonon modes in a crystal, the $\theta_D$ value implies greater energy needed to excite phonons, making this material well-suited for thermoelectric power generation. Moreover, a Debye temperature of 300 K or higher indicates high thermal conductivity in the crystal.[38] Given that the compound under investigation exhibits a Debye temperature of 192.8 K, we can conclude that it possesses high thermal conductivity.

The following empirical relation was used to compute the melting point of the compounds:[31]

$$T_{melt} = 607 + 9.3 \times B \pm 555 \quad (13)$$

According to this equation, the higher melting temperature of $Ti_2FeAs$ can be attributed to its higher bulk modulus. These findings are consistent with the methodology employed in previous ref. 17 for calculating mechanical properties. The computed formation energies and mechanical properties for $Ti_2FeAs$ are in agreement with that of other theoretically predicted Heusler alloys, as reported in ref. 52.

### 3.3 Electronic properties

The electron spin polarisation (SP) of a substance at $E_F$ is defined as follows:

$$SP = \frac{\rho_\uparrow(E_f) - \rho_\downarrow(E_f)}{\rho_\uparrow(E_f) + \rho_\downarrow(E_f)} \times 100 \quad (14)$$

where $\rho_\uparrow(E_f)$, $\rho_\downarrow(E_f)$ represent the densities of states for the majority and minority spins at the Fermi energy. The alloys are considered as true half-metallic when one of the densities of states from the majority or minority spins is zero, while the other is non-zero at the Fermi level $E_f$.

To explain the electronic structure of the considered alloy, we employed the optimized lattice constant within the lowest energy structures. Using three different approximations, *i.e.*, LSDA, PBE-GGA, and TB-mBJ, the spin-polarized band structures along the high-symmetry direction ($W$–$L$–$G$–$X$–$W$–$K$) in the first Brillouin zone are plotted in Fig. 3(a)–(c), respectively. Fig. 3 displays the electronic band structures for both spins and confirms the half-metallic nature of the material. It can be observed from Fig. 3(a) that according to the LSDA and GGA-PBE approximations, the conduction and valence bands overlap at the Fermi level in both spins, indicating the metallic behaviour of $Ti_2FeAs$. However, given that LSDA and PBE-GGA often underestimate the band structure, we employed the improved TB-mBJ functional to reveal the presence of a gap in the spin-down channels of the $Ti_2FeAs$ alloy. It was confirmed that LSDA and PBE-GGA do not show 100% spin polarization at $E_F$; however, when treated with mBJ, it showed 100% spin polarization. According to Fig. 3, it is evident that $Ti_2FeAs$ retains its half-metallic (HM) character with an increased value of band gap in the minority spin state, which is approximately 1.005 eV, and a half-metallic band gap of 0.739 eV. A similar trend was observed for the TB-mBJ approximation, where the spin-up states exhibit conducting behaviour, while the spin-down states behave as a semiconductor. As a result of the majority spin states anchoring the Fermi level, the band structure of $Ti_2FeAs$ demonstrates metallic characteristics. Conversely, in the minority spin state, the Fermi level resides within a band gap. Based on our findings, we can conclude that $Ti_2FeAs$ is a highly robust half-metallic ferromagnetic alloy, featuring an HM gap of 0.739 eV. This value is notably larger than the HM gaps reported in the literature for other Ti-based half-Heusler alloys, such as $Ti_2FeSi$, $Ti_2VAl$, $Ti_2VGa$, $Ti_2VIn$, $Ti_2FeGe$ and $Ti_2FeSn$, which exhibit HM gaps of 0.45 eV, 0.52 eV, 0.51 eV, 0.59 eV, and 0.60, respectively.[50–52] Briefly, the band structures of $Ti_2FeAs$ exhibit semiconducting character, with 100% spin polarization at the Fermi level, indicating the full half-metallic nature of the $Ti_2FeAs$ alloy.

### 3.4 Density of states

In general, the utilization of DOS spectral curves is valuable for providing a detailed description and explanation of the electronic structure of a material. Fig. 4(a) and (b) display the calculated spin-polarized total density of states (DOS) for the $Ti_2FeAs$ alloy at its equilibrium state by LDA, PBE-GGA and mBJ-GGA. It can be clearly observed in Fig. 4(a) and (b) that the system is not an HMF given that its $E_F$ is not located in the gap of the minority spin with both LSDA and PBE-GGA


© 2024 The Author(s). Published by the Royal Society of Chemistry

Open Access Article. Published on 23 February 2024. Downloaded on 2/5/2026 12:43:03 AM.
This article is licensed under a Creative Commons Attribution-NonCommercial 3.0 Unported Licence.

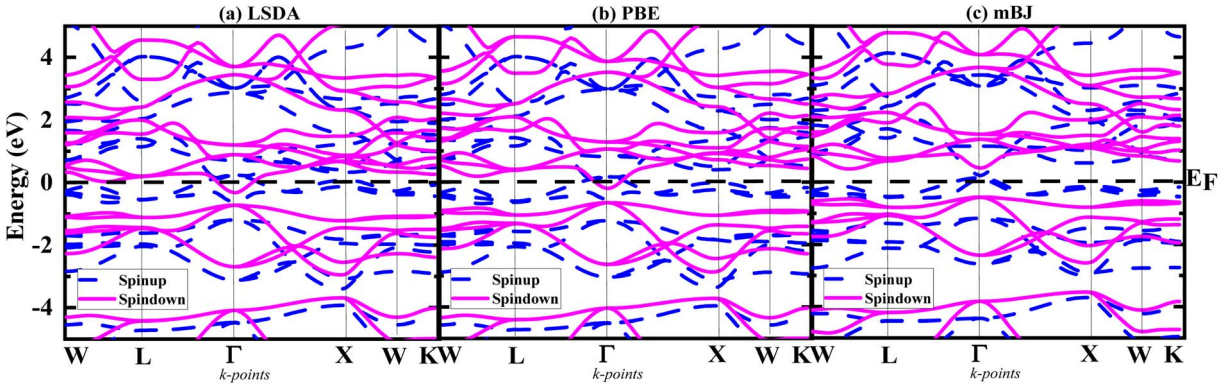


Fig. 3 Band structures of majority spin up and minority spin down of $Ti_2FeAs$for (a) LSDA, (b) PBE and (c) mBJ approximation.

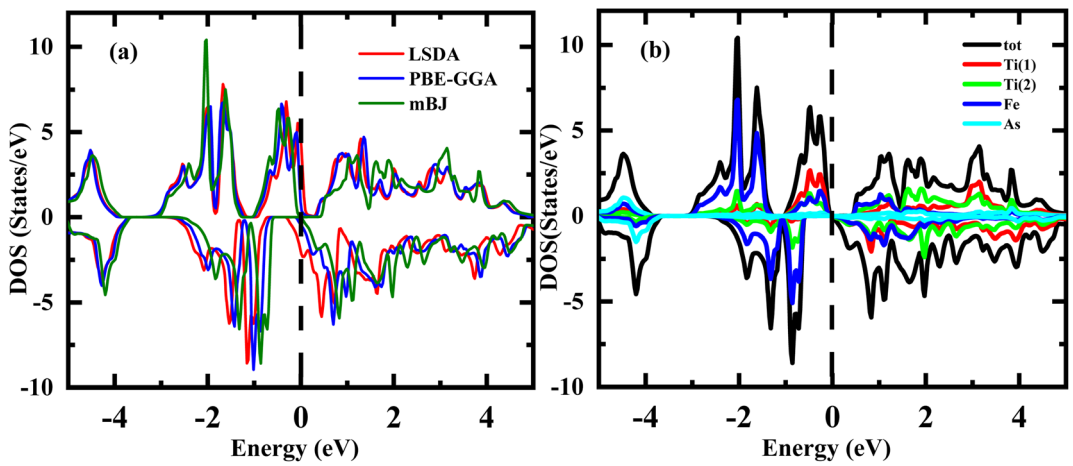


Fig. 4 Spin-polarized (a and b) total densities of states of majority spin (up) and minority spin (dn) for $Ti_2FeAs$ alloy, respectively.

approximations but becomes an HMF system when treated with the mBJ-GGA method.

Several findings can be concluded from the partial density of states (PDOS) analysis of the $Ti_2FeAs$ alloy, as shown in Fig. 5. The energy bands in the $Ti_2FeAs$ alloy, for both the majority and minority spin states, can be divided into three distinct regions. The energy bands in the vicinity of the Fermi level, spanning approximately $-5$ to 5 eV, are primarily associated with the d states ($t_{2g}$) at the Ti(1), Ti(2), and Fe atoms. Additionally, the energy bands within the range of $-4$ to 4 eV predominantly originate from the s and p states of the As atoms. The half-metallic (HM) nature of the $Ti_2FeAs$ alloy is confirmed by the existence of a majority state at the Fermi level and a band gap in the minority state. It is worth noting that the band gap in the HM region is due to the strong hybridization between the Ti(1)/Ti(2) atoms and the Fe atom.

To examine the characteristics of chemical bonding in the Heusler alloys,[62] we conducted an analysis of the charge density distribution and ELF along the (110) plane of the $Ti_2FeAs$ compound, as illustrated in Fig. 6. This plot reveals that there is a significant distribution of charge located between the TiAs atoms and between the FeAs atoms.

The calculated atomic magnetic moments for the LSDA, PBE-GGA and mBJ are presented in Table 3. The total magnetic moment ($M_{tot}$) of these alloys remains constant at 3.0 $\mu_B$ per formula unit in both the GGA and mBJ approximations. This consistency is in agreement with the Slater–Pauling equation[63] (SP), where $M_{tot} = Z_{tot} - 18$, indicating that $M_{tot}$ represents the total magnetic moment and $Z_{tot}$ represents the total number of valence electrons. In the case of $Ti_2FeAs$, $N$ is equal to 21. The calculated magnetic moment for $Ti_2FeAs$ yields an integer value of 3 $\mu_B$, corresponding to the $Hg_2CuTi$-type structure. This result is consistent with the predictions from the Slater–Pauling rule, indicating the potential for half-metallicity in the present case.

The magnetic moment of $Ti_2FeAs$ is zero due to the interplay between the 3d electrons of iron and the 3d electrons of titanium, which align in opposite directions and cancel the overall moment. The $M_{tot}$ in the $Ti_2FeAs$ alloy is comprised of contributions from four entities: Ti(1), Ti(2), Fe, and As atoms. Analysis of the interstitial region reveals that in principle, the participation originates from the $M_{tot}$ of the Ti(1) atoms. The Ti(1) and Ti(2) atoms exhibit positive magnetic moments, while the Fe atom shows a negative magnetic moment. The As atoms contribute minimally to the overall magnetic moment, with very small values.[64]

Open Access Article. Published on 23 February 2024. Downloaded on 2/5/2026 12:43:03 AM.
This article is licensed under a Creative Commons Attribution-NonCommercial 3.0 Unported Licence.

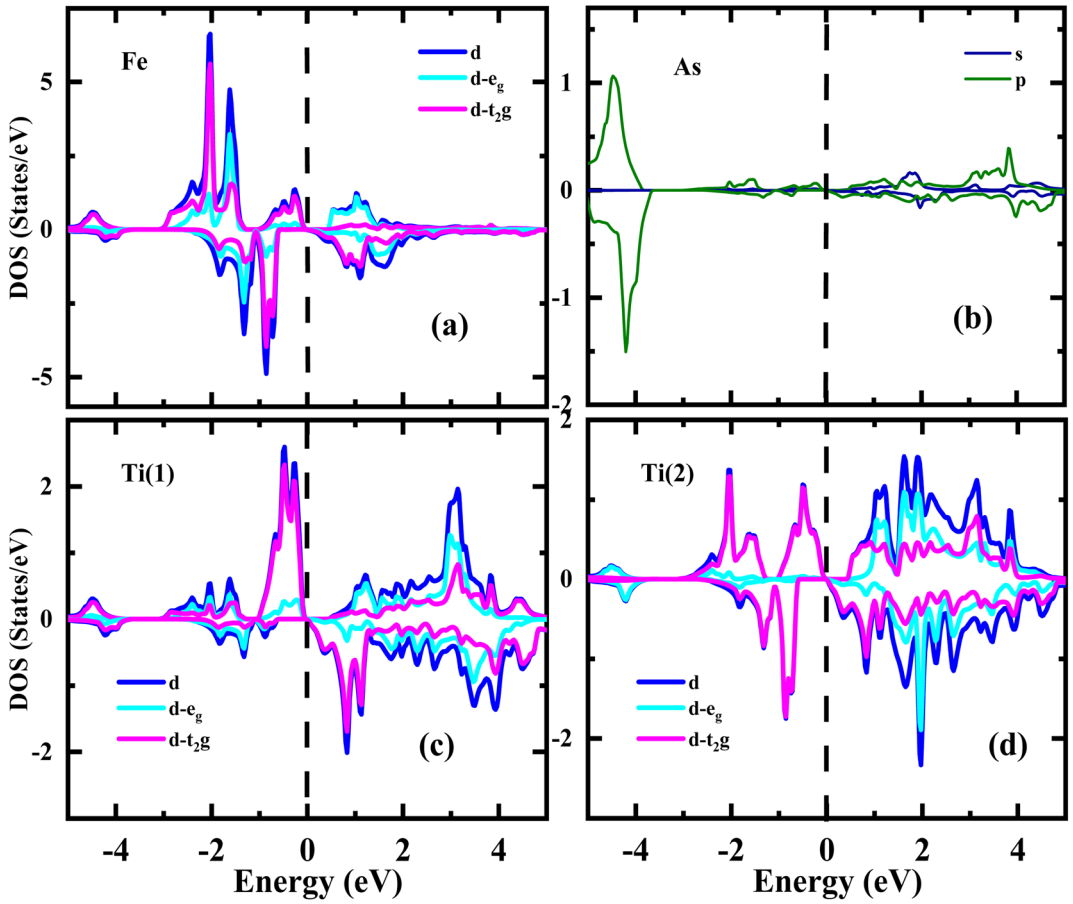


Fig. 5 Spin-polarized partial densities of states of majority spin (up) and minority spin (dn) for $Ti_2FeAs$ alloy for Fe (a), As (b), Ti(1) (c) and Ti(2) (d).

The Curie temperature will be discussed in the next section because it is crucial in real-world use. In comparison to the state with spin polarisation, the calculations for the paramagnetic state without spin polarisation demonstrate a superior total energy value. The Curie temperature can be described using the nearest neighbour Heisenberg model within the conventional statistical approach. In this context, the simplest mean-field approximation (MFA) is employed. According to the MFA, the Curie temperature is the temperature at which the average magnetic moment of a three-dimensional Heisenberg ferromagnet cancels out. Consequently, the energy difference between the ferromagnetic ground state and the nonmagnetic state directly provides an estimate of the TMFA $C$ value. Subsequently, this relation was employed to determine the transition temperature of the standard three-dimensional Heisenberg ferromagnet within the mean-field approximation,[65] as follows:

$$T_C^{MFA} = \frac{2}{3}\frac{\Delta E}{K} \quad (15)$$

where $\Delta E$ represents the energy needed to align adjacent slabs in a ferromagnetic manner and $K$ denotes the Boltzmann constant. Using these parameters, the calculated Curie temperature for $Ti_2FeAs$ was determined to be 566 K, corresponding to the lattice parameter ($a_0$) obtained from volume optimization. This Curie temperature exceeds the temperature typically associated with room temperature.[66,67]

### 3.5 Thermodynamic properties

The thermodynamic properties of $Ti_2FeAs$ were determined using the quasi-harmonic Debye model, which utilizes the non-equilibrium Gibbs function $G^*(V;P,T)$.[68]

$$G^*(V;P,T) = E(V) + PV + A_{vib}[V,T] \quad (16)$$

where $E(V)$ is the total energy of the crystal and $PV$ is the constant hydrostatic condition. The vibrational term $A_{vib}$ can be considered and understood from ref. 69 and 70.

The thermal characteristics were computed in the temperature range of 0 to 1200 K. Also, the effect of pressure was calculated in the range of 0 to 180 GPa.

Fig. 7(a) depicts the correlation between the bulk modulus and pressure, showing linearity in the temperature range of 0 to 1200 K. At a given temperature, the bulk modulus of the $Ti_2FeAs$ alloy increases with pressure, whereas it decreases with temperature at a given pressure, exhibiting similar behaviour. The bulk modulus represents a measure of the resistance of the compound to volume change when subjected to compression.

In the temperature range of 0 to 100 K, the bulk modulus ($B$) remains nearly constant. However, for temperatures above 100


© 2024 The Author(s). Published by the Royal Society of Chemistry

Open Access Article. Published on 23 February 2024. Downloaded on 2/5/2026 12:43:03 AM.
This article is licensed under a Creative Commons Attribution-NonCommercial 3.0 Unported Licence.

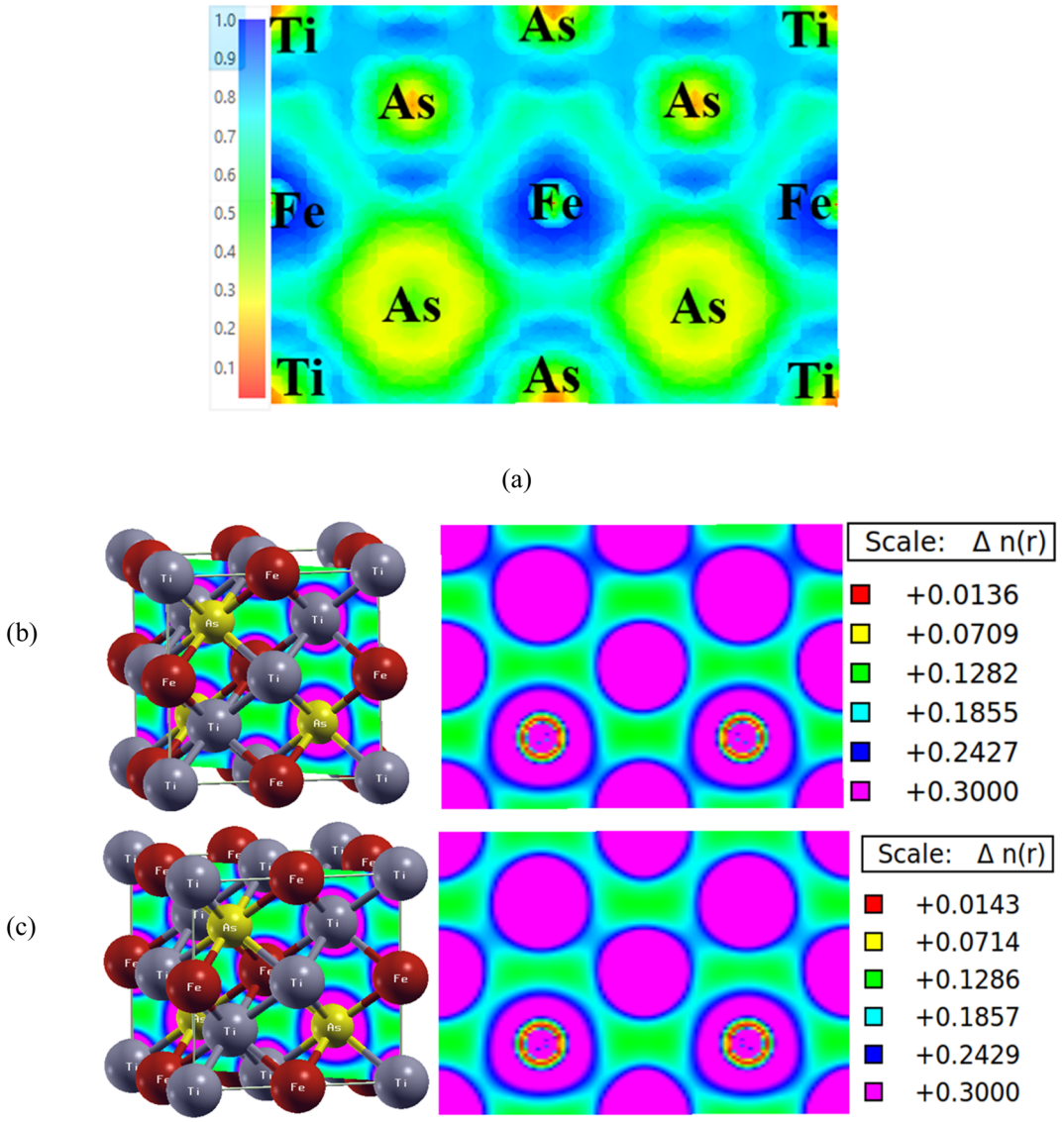


Fig. 6 (a) Electron localization function (ELF) along the 110 plane and plot of charge density distribution along the (110) plane of $Ti_2FeAs$ compound for (b) spin up and (c) spin down, respectively.

Table 3 The total and atomic magnetic moments of the $Ti_2FeAs$ compound by different exchange–correlation potentials (XC) (LSDA, PBE-GGA and mBJ-GGA). $M_{tot}$ ($\mu_B$): total magnetic moment; $M_{Ti}$ ($\mu_B$): Ti magnetic moment; $M_{Ti}$ ($\mu_B$): Ti magnetic moment; $M_{Fe}$ ($\mu_B$): Fe magnetic moment; $M_{As}$ ($\mu_B$): As magnetic moment; and $M_{int}$ ($\mu_B$): the magnetic moment in the interstitial region

| $Ti_2FeAs$ | Magnetic moments | | |
|---|---|---|---|
| XC | LSDA | PBE | mBJ |
| $M_{int}$ ($\mu_B$) | 0.42059 | 0.47275 | 0.38518 |
| $M_{Ti}$ ($\mu_B$) | 1.05515 | 1.27260 | 1.29355 |
| $M_{Ti}$ ($\mu_B$) | 0.32871 | 0.38989 | 0.30102 |
| $M_{Fe}$ ($\mu_B$) | 0.66295 | 0.79218 | 1.01465 |
| $M_{As}$ ($\mu_B$) | 0.02388 | 0.02199 | 0.00579 |
| $M_{tot}$ ($\mu_B$) | 2.49127 | 2.94942 | 3.00020 |

K, at a constant pressure, $B$ declines linearly as the temperature increases. Additionally, at a specific temperature, the compressibility grows significantly with pressure, suggesting that the $Ti_2FeAs$ structure becomes more malleable as it enters a new bonding arrangement. At the earliest state of zero temperature and pressure, the estimated bulk modulus is 157.50 GPa, which is reasonably consistent with the value of 153.641 GPa obtained from structural characteristic. Furthermore, at 300 K and zero pressure, the measured bulk modulus is 88.21 GPa. These observations indicate that the studied material exhibits significant compressibility and strong hardness.

Fig. 7(b) illustrates the variation in the unit cell volume with temperature at a fixed pressure in the range of 0 to 180 GPa. It is evident that at a given temperature, the volume decreases as the pressure increases. Conversely, at a given pressure, the volume shows a very slow increase with temperature. Analysis of the data in Fig. 7(b) reveals that the determined volume for $Ti_2FeAs$

Open Access Article. Published on 23 February 2024. Downloaded on 2/5/2026 12:43:03 AM.
This article is licensed under a Creative Commons Attribution-NonCommercial 3.0 Unported Licence.

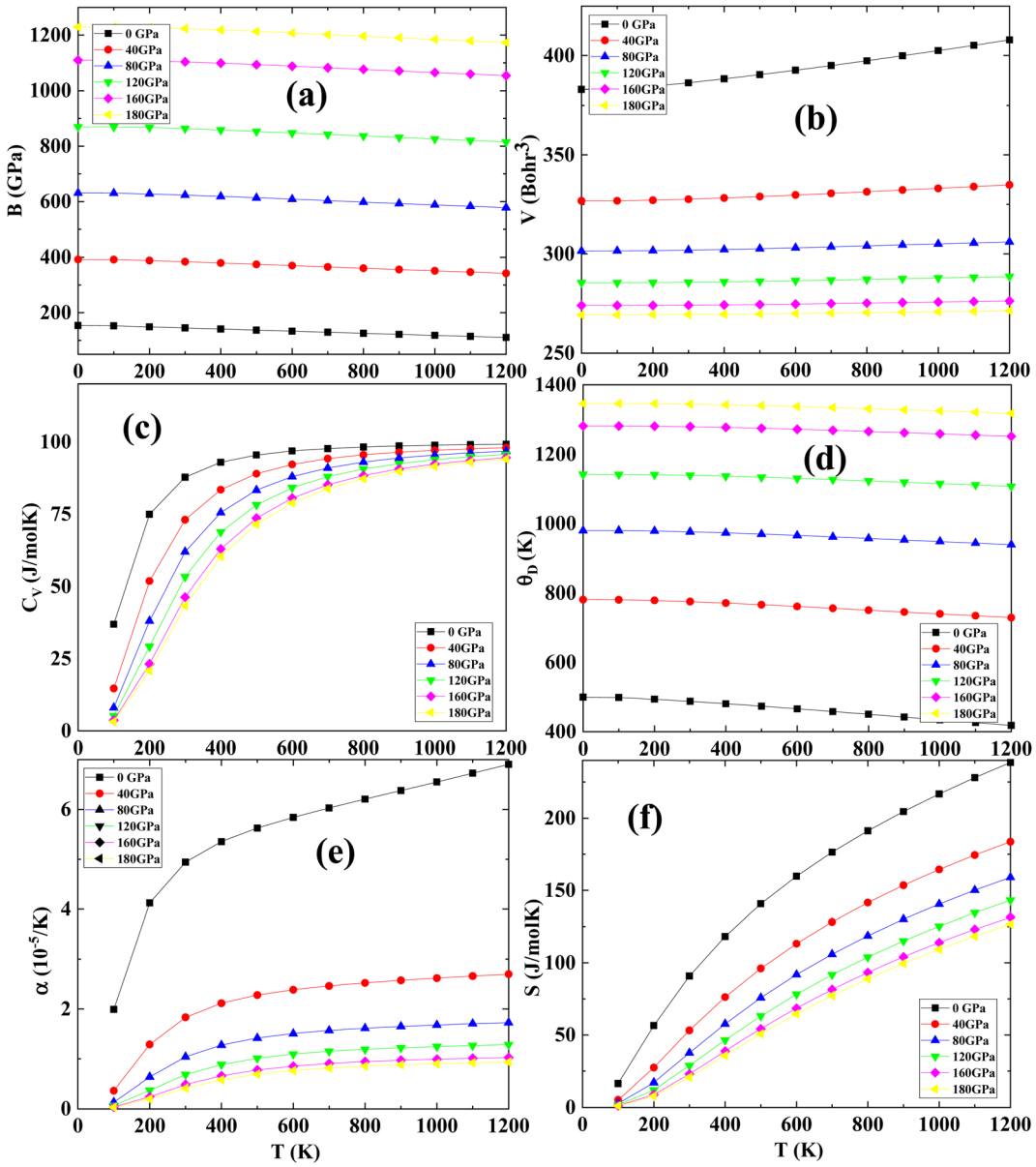


Fig. 7 Variation in different thermodynamic parameters as a function of temperature and pressure. (a) Bulk modulus, $B$, (b) unit cell volume, $V$, (c) heat capacity at constant volume, $C_V$, (d) Debye temperature, $\theta_D$, (e) thermal expansion coefficient, $\alpha$, and (f) entropy, $S$.

at zero pressure and zero temperature is 346.17 bohr$^3$, which agrees well with the data obtained from the structural properties (344.795 bohr$^3$).

The specific heat capacity ($C_v$) is a crucial parameter that provides valuable insights into the motion of molecules, lattice vibration, and phase transitions in crystals. Fig. 7(c) illustrates the relationship between $C_v$ and temperature at various pressure values for the $Ti_2FeAs$ compound. It can be observed that $C_v$ exhibits a rapid increase with temperature, following the Debye law ($C_v \propto T^3$).[71] As the temperature reaches 600 K, the rate of increase in $C_v$ is slow, eventually approaching a value of 75 J mol$^{-1}$ K$^{-1}$. This value corresponds to the Dulong–Petit classical limit, which is a common phenomenon observed in all solids.[72]

In the quasi-harmonic method, the Debye temperature ($\theta_D$) serves as a fundamental parameter, which provides valuable insights into various physical characteristics of solids, including elastic constants, specific heat, and melting temperature. Within the quasi-harmonic Debye model, the highest parameter concerning crystal vibration is $\theta_D$. Fig. 7(d) illustrates the relationship between pressure and $\theta_D$ at a constant temperature. It can be observed that increasing the pressure from 0 to 180 GPa leads to an augmentation in $\theta_D$, while it decreases linearly with temperature. At room temperature and 0 GPa, $\theta_D$ was estimated to be approximately 201.65 K.[73]

Additionally, the thermal expansion coefficient ($\alpha$), which characterizes the propensity of a material to change size with a variation in temperature, was calculated. Fig. 7(e) displays the variation in the thermal expansion coefficient ($\alpha$) as a function of temperature at a pressure in the range of 0 to 180 GPa, where $\alpha$ exhibits a linear increase with temperature up to 400 K,


© 2024 The Author(s). Published by the Royal Society of Chemistry

Open Access Article. Published on 23 February 2024. Downloaded on 2/5/2026 12:43:03 AM.
This article is licensed under a Creative Commons Attribution-NonCommercial 3.0 Unported Licence.

particularly at 0 GPa. However, at high temperatures ($T > 400$ K), the rate of increase slows down, eventually converging to a constant value.[74] Fig. 7(e) demonstrates that pressure has the opposite effect on the coefficient of thermal expansion; as pressure increases, the thermal expansion decreases. At a temperature of 400 K and pressure of 0 GPa, the coefficient of thermal expansion ($\alpha$) was measured to be $2.56 \times 10^{-5}$ $K^{-1}$. On average, the values of the thermal expansion coefficient at 0 GPa range from about $22.6 \times 10^{-5}$ $K^{-1}$ at ambient temperature to approximately $54 \times 10^{-5}$ $K^{-1}$ at 1200 K.[75] This behaviour can be attributed to the influence of the harmonic term in the cohesive energy, which governs the small displacements of the atom around its equilibrium position.

The entropy ($S$) is a significant thermodynamic property that is subjected to investigation. It provides crucial insights into the vibrational properties of a material and describes the precise physical state of a system. Entropy plays a vital role in the functioning of various devices, including refrigerators, heat pumps, and heat engines. Fig. 7(f) presents the variation in entropy ($S$) as a function of temperature at different pressures for $Ti_2FeAs$. Observing the curves, it can be noted that they originate from an entropy value of zero at 0 K and 0 GPa. Subsequently, as the temperature increases, the entropy rises exponentially. Under the conditions of 300 K and 0 GPa, the entropy reaches a value of 80.38 J $mol^{-1}$ $K^{-1}$. Additionally, for temperatures exceeding 700 K, the entropy becomes

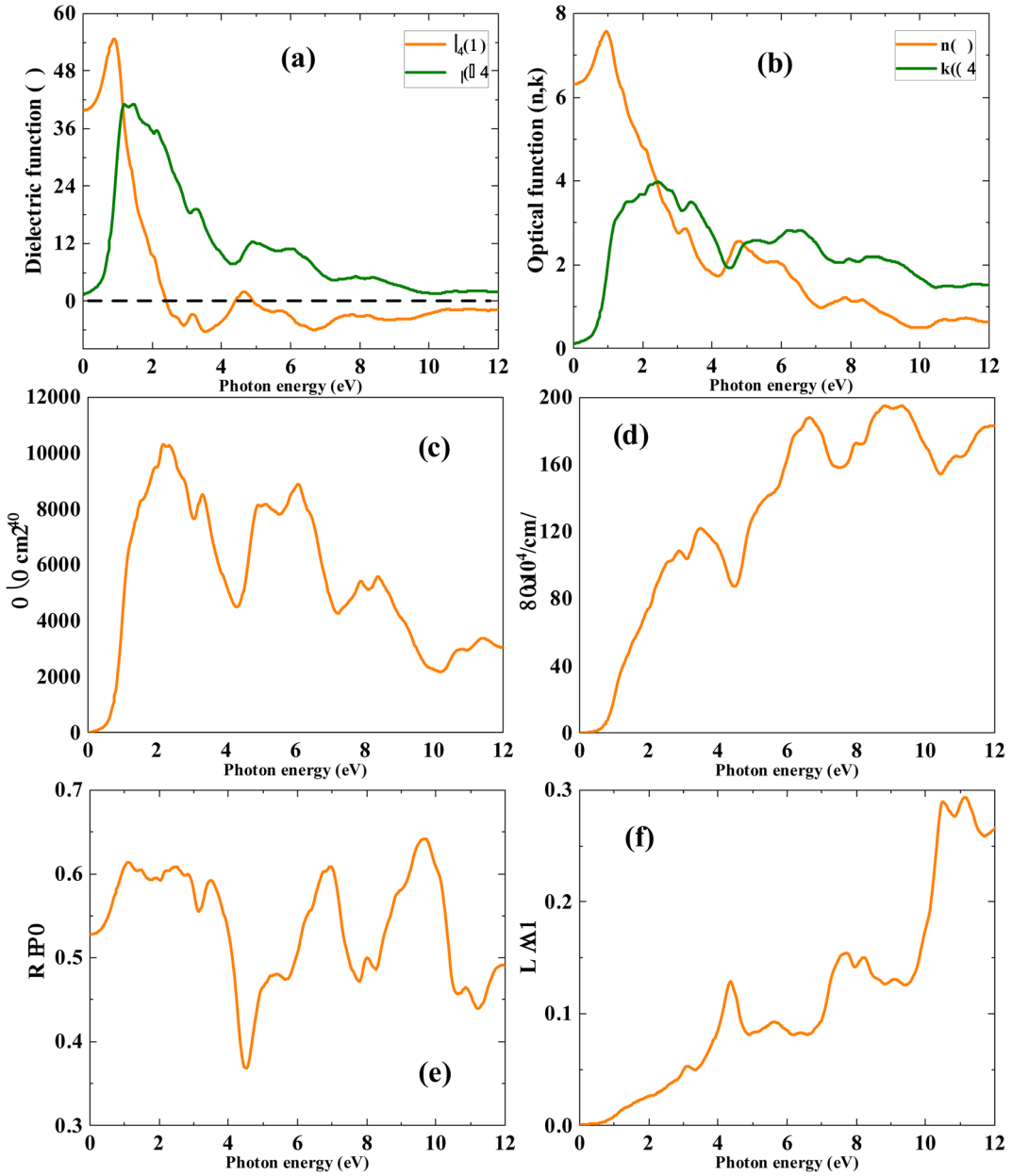


Fig. 8 Variation in different optical parameters as a function of photon energy. (a) Dielectric function, $\varepsilon$, (b) optical function, (c) optical conductivity, $\sigma$, (d) absorption coefficient, $\alpha$, (e) reflectivity, $R$, and (f) energy loss spectra, $L$.

Open Access Article. Published on 23 February 2024. Downloaded on 2/5/2026 12:43:03 AM.
This article is licensed under a Creative Commons Attribution-NonCommercial 3.0 Unported Licence.

significantly high. This indicates that elevated temperatures contribute to an increase in the vibrational entropy of the material, while simultaneously decreasing its cohesive energy.[76]

### 3.6 Optical properties

The development of optical technology and its applications depends on exact and reliable measurements of the optical characteristics of materials. These measurements include dielectric functions, index of refraction, optical conduction, absorbance, reflectance, transmittance, and emittance. The electronic band structure of a material mostly affects its optical characteristics. Consequently, optical investigations are frequently employed to determine the electronic band structure of solids in a quantitative manner. In this regard, the optical performance of $Ti_2FeAs$ was examined using the WIEN2k code.

Firstly, the dielectric function $\varepsilon(\omega)$ provides valuable insights into the optical properties of a material, given that it quantifies the linear response of the system to an external electromagnetic field, as described by the following equation:[77]

$$\varepsilon(\omega) = \varepsilon_1(\omega) + i\varepsilon_2(\omega). \quad (17)$$

The formula for the imaginary part $\varepsilon_2(\omega)$ is

$$\varepsilon_2 = \frac{{\omega_p}^2}{8\pi^3 c^3 \tau}\lambda^3 \quad (18)$$

Moreover, the Kramers–Kronig transformation (KKT) gives the value of the real part of $\varepsilon(\omega)$ *i.e.* $\varepsilon_1(\omega)$

$$\varepsilon_1(\omega) = 1 + \frac{2}{\pi} M \int_0^\infty \frac{\omega' \varepsilon_2(\omega')}{\omega'^2 - \omega^2} d\omega' \quad (19)$$

We also calculated the refractive index $n(\omega)$ acquired in connection with the complex dielectric function as follows:[78]

$$n(\omega) = \frac{1}{\sqrt{2}}\left(\varepsilon_1 + \left({\varepsilon_1}^2 + {\varepsilon_2}^2\right)^{1/2}\right)^{1/2} \quad (20)$$

The reflectivity $R(\omega)$ of $Ti_2FeAs$ is obtained directly from $\varepsilon_1(\omega)$ and $\varepsilon_2(\omega)$.

Fig. 8(a) illustrates the real and imaginary components of the total dielectric function for $Ti_2FeAs$. The presence of peaks in these components can be attributed to the transitions occurring in the spin-down channel, as deduced from the analysis of the band structure and density of states (DOS). Notably, the calculated values of the real component $\varepsilon_1(\omega)$ at (0 eV) exhibit striking similarity. Furthermore, the significant magnitude of the imaginary component of the dielectric function, $\varepsilon_2(\omega)$, serves as evidence for the metallic nature of the compounds.

The refractive index of a material plays a crucial role in photoelectric applications. Fig. 8(b) depicts the refractive index of $Ti_2FeAs$, showing peaks in the lower energy region, which gradually approach zero in the visible domain. These peaks originate from interband transitions between the valence and the conduction band. The presence of peaks in the infrared region indicates nonlinear behaviour in the refractive index. Additionally, a few smaller peaks are observed at higher energies due to this nonlinearity. The optical conductivity depicted in Fig. 8(c) characterizes the metallic behaviour of the material, emphasizing its ability to conduct light.

Fig. 8(d) displays the absorption coefficients, indicating the presence of peaks in the high energy region. Further, according to this figure, the absorption of photons occurs in the range of 3–4 eV and mostly in the higher energy side of 6–9 eV (UV-region).

Fig. 8(e) presents the reflectivity, showing the maximum reflectivity in the lower energy region. The reflectivity remains relatively constant in the intermediate energy range, but a peak is also observed at higher energies. Furthermore, the real part of the dielectric function ($\varepsilon_1(\omega)$) becomes negative for energetic photons, resulting in reflectivity peaks. This observation further confirms the metallic nature of the compound, given that it exhibits an energy range where it becomes highly reflective to incident photons.

## 4. Conclusion

The structural, mechanical, electronic, optical, thermodynamic and magnetic properties of the $Ti_2FeAs$ alloy of the $Hg_2CuTi$-type structure were investigated using DFT calculations. We carried out our analysis within the modified Becke and Johnson potential (mBJ) exchange–correlation potential, the generalised gradient approximation (GGA), and LDA using the first-principles plane-wave (FP-LAPW) technique. Additionally, the mechanical stability of the $Ti_2FeAs$ alloy was determined by its high melting temperatures. Our calculations demonstrated that $Ti_2FeAs$ exhibits characteristics of a half-metallic (HMF) ferromagnet with a spin-gap value of 0.739 eV, as evidenced by the electronic band structure calculations. At the equilibrium volume for mBJ approximations, the compound possesses a magnetic moment of 3.0 $\mu_B$ per formula unit. The analysis of the real and imaginary parts of the dielectric function, reflectivity, and optical conductivity revealed that the compound displays optical metallic behavior, as reflected in the imaginary part of the dielectric function ($\varepsilon_2$). The alloy exhibits optical activity at both lower and higher energies, indicating its highly nonlinear nature. The magnetic moments are reasonably consistent with the Slater–Pauling rule, confirming 100% spin polarization at the Fermi level, which is crucial for spintronic applications. The structural optimization further established the stability of the compound and satisfies the requirement of a relatively high Curie temperature. The heat capacity, thermal expansion, Debye temperature, and entropy factors were all calculated. Furthermore, neither experimental nor theoretical data are available for this compound; however, it is anticipated that these data will validate the present numerical data. Therefore, the full-Heusler metal $Ti_2FeAs$ would be significant in the applications of spintronics, design cues and UV-absorber.

## Conflicts of interest

There are no conflicts to declare.


© 2024 The Author(s). Published by the Royal Society of Chemistry

Open Access Article. Published on 23 February 2024. Downloaded on 2/5/2026 12:43:03 AM. This article is licensed under a Creative Commons Attribution-NonCommercial 3.0 Unported Licence.

## Acknowledgements

The authors extend their appreciation to the Deanship of Scientific Research at King Khalid University (Abha, Saudi Arabia) for funding this work through Research Groups Program under grant number (RGP.2/60/44).

## References

1 M. N. Baibich, J. M. Broto, A. Fert, F. N. V. Dau, F. Petroff, P. Etienne, G. Creuzet, A. Friederich and J. Chazelas, Giant magnetoresistance of (001) Fe/(001) Cr magnetic superlattices, *Phys. Rev. Lett.*, 1988, **61**(21), 2472.

2 N. Kaur, V. Srivastava, S. A. Dar, R. Khenata and R. Sharma, A unified DFT exploration on transport and thermodynamic properties of L21 structure of Rh2XZn (X = Mn, Fe) ferromagnets, *Mater. Sci. Eng., B*, 2023, **287**, 116099.

3 N. Kaur, V. Srivastava and S. A. Dar, GGA based study on electronic structure and thermoelectric properties of $Mn_2PtCo$ full-Heusler compound, *Indian J. Phys.*, 2022, **96**(1), 71–77.

4 S. Pawar, H. Duadi and D. Fixler, Recent Advances in the Spintronic Application of Carbon-Based Nanomaterials, *Nanomaterials*, 2023, **13**(3), 598.

5 B. Dieny, I. L. Prejbeanu, K. Garello, P. Gambardella, P. Freitas, R. Lehndorff, W. Raberg, *et al.*, Opportunities and challenges for spintronics in the microelectronics industry, *Nat. Electron.*, 2020, **3**(8), 446–459.

6 S. A. Chambers and Y. K. Yoo., New materials for spintronics, *MRS Bull.*, 2003, **28**(10), 706–710.

7 G. Schmidt, D. Ferrand, L. W. Molenkamp, A. T. Filip and B. J. Van Wees, Fundamental obstacle for electrical spin injection from a ferromagnetic metal into a diffusive semiconductor, *Phys. Rev. B: Condens. Matter Mater. Phys.*, 2000, **62**(8), R4790.

8 R. Fiederling, M. Keim, G. a. Reuscher, W. Ossau, G. Schmidt, A. Waag and L. Molenkamp, *Nature*, 1999, **402**, 787.

9 Y. Ohno, D. K. Young, B. Beschoten, F. Matsukura, H. Ohno and D. D. Awschalom, Electrical spin injection in a ferromagnetic semiconductor heterostructure, *Nature*, 1999, **402**(6763), 790–792.

10 R. A. De Groot, F. M. Mueller, P. G. V. van Engen and K. H. J. Buschow, New class of materials: half-metallic ferromagnets, *Phys. Rev. Lett.*, 1983, **50**(25), 2024.

11 K.-I. Kobayashi, T. Kimura, H. Sawada, K. Terakura and Y. Tokura, Room-temperature magnetoresistance in an oxide material with an ordered double-perovskite structure, *Nature*, 1998, **395**(6703), 677–680.

12 G. D. Liu, X. F. Dai, H. Y. Liu, J. L. Chen, Y. X. Li, G. Xiao and G. H. Wu, $Mn_2Coz$ (z = Al, Ga, In, Si, Ge, Sn, Sb) compounds: structural, electronic, and magnetic properties, *Phys. Rev. B: Condens. Matter Mater. Phys.*, 2008, **77**(1), 014424.

13 K. Özdoğan, E. Şaşıoğlu, B. Aktaş and I. Galanakis, Doping and disorder in the $Co_2MnAl$ and $Co_2MnGa$ half-metallic Heusler alloys, *Phys. Rev. B: Condens. Matter Mater. Phys.*, 2006, **74**(17), 172412.

14 H. Luo, G. Liu, F. Meng, J. Li, E. Liu and G. Wu, Half-metallicity in Fe-based Heusler alloys $Fe_2TiZ$ (Z = Ga, Ge, As, In, Sn and Sb), *J. Magn. Magn. Mater.*, 2012, **324**(20), 3295–3299.

15 C. M. Aerts, P. Strange, M. Horne, W. M. Temmerman, Z. Szotek and A. Svane, Half-metallic to insulating behavior of rare-earth nitrides, *Phys. Rev. B: Condens. Matter Mater. Phys.*, 2004, **69**(4), 045115.

16 V. Srivastava, N. Kaur, X. Wang, M. Mushtaq and S. Ahmad Dar, First-principles study on structural, electronic, magnetic, elastic, mechanical and thermodynamic properties of $Mn_2PtCo$ Heusler alloy, *Int. J. Energy Res.*, 2021, **45**(7), 11305–11319.

17 V. Srivastava, N. Kaur, R. Khenata and S. A. Dar, *J. Magn. Magn. Mater.*, 2020, **513**, 167107.

18 H. P. J. Wijn, Alloys and compounds of 3d elements with main group elements, in *Magnetic Properties of Metals: D-Elements, Alloys and Compounds*, Springer Berlin Heidelberg, Berlin, Heidelberg, 1988, pp. 95–158.

19 K. R. A. Ziebeck and K. U. Neumann, *Magnetic properties of metals, Landolt-Bornstein III*, 2001, vol. 32.

20 R. J. Soulen Jr, J. M. Byers, M. S. Osofsky, B. Nadgorny, T. Ambrose, S. F. Cheng, P. R. Broussard, *et al.*, Measuring the spin polarization of a metal with a superconducting point contact, *Science*, 1998, **282**(5386), 85–88.

21 C. Ciccarelli, L. Anderson, V. Tshitoyan, A. J. Ferguson, F. Gerhard, C. Gould, L. W. Molenkamp, *et al.*, Room-temperature spin–orbit torque in NiMnSb, *Nat. Phys.*, 2016, **12**(9), 855–860.

22 K. A. Kilian and R. H. Victora, Electronic structure of $Ni_2MnIn$ for use in spin injection, *J. Appl. Phys.*, 2000, **87**(9), 7064–7066.

23 Ch Hordequin, J. P. Nozieres and J. Pierre, Half metallic NiMnSb-based spin-valve structures, *J. Magn. Magn. Mater.*, 1998, **183**(1–2), 225–231.

24 S. Ishida, S. Fujii, S. Kashiwagi and S. Asano, Search for half-metallic compounds in $Co_2MnZ$ (Z = IIIb, IVb, Vb element), *J. Phys. Soc. Jpn.*, 1995, **64**(6), 2152–2157.

25 S. Fujii, S. Sugimura and S. Asano, Hyperfine fields and electronic structures of the heusler alloys Co2MnX (X = Al, Ga, Si, Ge, Sn), *J. Phys.: Condens. Matter*, 1990, **2**(43), 8583.

26 S. Fujii, S. Ishida and S. Asano, A half-metallic band structure and $Fe_2MnZ$ (Z = Al, Si, P), *J. Phys. Soc. Jpn.*, 1995, **64**(1), 185–191.

27 H. P. J. Wijn, Alloys and compounds of 3d elements with main group elements, in *Magnetic Properties of Metals: D-Elements, Alloys and Compounds*, Springer Berlin Heidelberg, Berlin, Heidelberg, 1988, pp. 95–158.

28 H. C. Kandpal, G. H. Fecher, C. Felser and G. Schönhense, Correlation in the transition-metal-based Heusler compounds $Co_2MnSi$ and $Co_2FeSi$, *Phys. Rev. B: Condens. Matter Mater. Phys.*, 2006, **73**(9), 094422.

29 X.-P. Wei, J.-B. Deng, G.-Y. Mao, S.-B. Chu and X.-R. Hu, Half-metallic properties for the Ti2YZ (Y = Fe, Co, Ni, Z = Al, Ga, In) Heusler alloys: a first-principles study, *Intermetallics*, 2012, **29**, 86–91.

© 2024 The Author(s). Published by the Royal Society of Chemistry

Open Access Article. Published on 23 February 2024. Downloaded on 2/5/2026 12:43:03 AM. This article is licensed under a Creative Commons Attribution-NonCommercial 3.0 Unported Licence.

30 N. Zheng and Y. Jin, Band-gap and Slater–Pauling rule in half-metallic $Ti_2$-based Heusler alloys: a first-principles study, *J. Magn. Magn. Mater.*, 2012, **324**(19), 3099–3104.
31 H. M. Huang, S. J. Luo and K. L. Yao, First-principles study of half-metallic properties of the Heusler alloy $Ti_2CoGe$, *J. Magn. Magn. Mater.*, 2012, **324**(16), 2560–2564.
32 I. Galanakis, P. H. Dederichs and N. Papanikolaou, Slater-Pauling behavior and origin of the half-metallicity of the full-Heusler alloys, *Phys. Rev. B: Condens. Matter Mater. Phys.*, 2002, **66**(17), 174429.
33 I. Galanakis, and P. H. Dederichs, Half-metallicity and Slater-Pauling behavior in the ferromagnetic Heusler alloys, *Half-Metallic Alloys: Fundamentals and Applications*, 2005, pp. 1–39.
34 K. R. A. Ziebeck and K. U. Neumann, *Magnetic properties of metals, Landolt-Bornstein III*, vol. 32, 2001.
35 I. Galanakis, K. Özdoğan, B. Aktaş and E. Şaşıoğlu, Effect of doping and disorder on the half metallicity of full Heusler alloys, *Appl. Phys. Lett.*, 2006, **89**(4), 042502.
36 A. Kumar and P. C. Srivastava, Synthesis and characterization of $Co_2FeAl$ Heusler alloy nanoparticles, *Mater. Sci.-Pol.*, 2013, **31**, 501–505.
37 N. Rabie, G. R. Gordani and A. Ghasemi, Enhancement of magnetic properties of $Co_2MnSi$ Heusler alloy prepared by mechanical alloying method, *J. Magn. Magn. Mater.*, 2017, **434**, 135–142.
38 K. R. Sapkota, P. Gyawali, A. Forbes, I. L. Pegg and J. Philip, Synthesis and characterization of $Co_2FeAl$ nanowires, *J. Appl. Phys.*, 2012, **111**, 123906.
39 J. H. Du, Y. L. Zuo, Z. Wang, J. H. Ma and L. Xi, Properties of $Co_2FeAl$ Heusler alloy nano-particles synthesized by coprecipitation and thermal deoxidization method, *J. Mater. Sci. Technol.*, 2013, **29**(3), 245–248.
40 K. Hotta, K. Nakamura, T. Akiyama, T. Ito, T. Oguchi and A. J. Freeman, Atomic-layer alignment tuning for giant perpendicular magnetocrystalline anisotropy of 3d transition-metal thin films, *Phys. Rev. Lett.*, 2013, **110**(26), 267206.
41 D. Behera, R. Sharma, H. Ullah, H. S. Waheed and S. K. Mukherjee, Electronic, optical, and thermoelectric investigations of Zintl phase $AAg_2Se_2$ (A = Sr, Ba) compounds: a first-principle approach, *J. Solid State Chem.*, 2022, **312**, 123259.
42 D. Behera, A.-R. Ahmed, A. Bouhenna, M. M. Salah, S. Ahmed and S. K. Mukherjee, First-Principles Studies on the Physical Properties of the Half Heusler RbNbCd and RbNbZn Compounds: A Promising Material for Thermoelectric Applications, *Crystals*, 2023, **13**(4), 618.
43 P. Kurz, G. Bihlmayer and S. Blügel, Magnetism and electronic structure of hcp Gd and the Gd (0001) surface, *J. Phys.: Condens. Matter*, 2002, **14**(25), 6353.
44 P. Hohenberg and W. Kohn, Inhomogeneous electron gas, *Phys. Rev.*, 1964, **136**(3B), B864.
45 K. Schwarz, P. Blaha and G. K. H. Madsen, Electronic structure calculations of solids using the WIEN2k package for material sciences, *Comput. Phys. Commun.*, 2002, **147**(1–2), 71–76.
46 J. P. Perdew, K. Burke and M. Ernzerhof, Generalized gradient approximation made simple, *Phys. Rev. Lett.*, 1996, **77**(18), 3865.
47 U. Von Barth and L. Hedin, A local exchange-correlation potential for the spin polarized case. i, *J. Phys. C: Solid State Phys.*, 1972, **5**(13), 1629.
48 F. Tran and P. Blaha, Accurate band gaps of semiconductors and insulators with a semilocal exchange-correlation potential, *Phys. Rev. Lett.*, 2009, **102**(22), 226401.
49 F. D. Murnaghan, The compressibility of media under extreme pressures, *Proc. Natl. Acad. Sci. U. S. A.*, 1944, **30**(9), 244–247.
50 M. Drief, Y. Guermit, N. Benkhettou, D. Rached, H. Rached and T. Lantri, First-Principles Study of Half-Metallic Ferrimagnet Behavior in Titanium-Based Heusler Alloys $Ti_2FeZ$ (Z = Al, Ga, and In), *J. Supercond. Novel Magn.*, 2018, **31**, 1059–1065.
51 S. Galehgirian and F. Ahmadian, First principles study on half-metallic properties of Heusler compounds $Ti_2VZ$ (Z = Al, Ga, and In), *Solid State Commun.*, 2015, **202**, 52–57.
52 X.-P. Wei, Ge-Y. Mao, S.-B. Chu, H. Deng, J.-B. Deng and X.-R. Hu, First-principles investigations of stability, electronic and thermodynamic properties of $Ti_2FeGe$ and $Ti_2FeSn$, *J. Magn. Magn. Mater.*, 2013, **341**, 122–128.
53 M. Pugaczowa-Michalska, Theoretical prediction of ferrimagnetism in $Mn_2FeB$, $Mn_2CoB$ and $Mn_2NiB$, *Intermetallics*, 2012, **24**, 128–134.
54 J. M. K. Al-zyadi, G. Y. Gao and K.-L. Yao, First-principles investigation of the structural and electronic properties of bulk full-Heusler alloy $Mn_2CoSn$ and its (001) surface, *J. Alloys Compd.*, 2013, **565**, 17–21.
55 M. Jamal, *IRelast and 2DR-optimize packages are provided by M. Jamal as Part of the Commercial Code WIEN2K*, 2014.
56 M. Born, K. Huang and M. Lax, Dynamical theory of crystal lattices, *Am. J. Phys.*, 1955, **23**(7), 474.
57 W. Voigt, On the relationship between the two elasticity constants of isotropic bodies, *Ann. Phys.*, 1889, **274**(12), 573–587.
58 A. Reuss, Calculation of the flow limits of mixed crystals on the basis of the plasticity of monocrystals, *Z. Angew. Math. Mech.*, 1929, **9**, 49–58.
59 R. Hill, *Proc. Phys. Soc., London, Sect. A*, 1952, **65**, 349.
60 S. F. Pugh, XCII. Relations between the elastic moduli and the plastic properties of polycrystalline pure metals, *Lond. Edinb. Dubl. Phil. Mag.*, 1954, **45**(367), 823–843.
61 I. N. Frantsevich, Elastic constants and elastic moduli of metals and insulators, *Reference Book*, 1982.
62 X. Qin and X. Yang, Theoretical design of $Ti_2$-based magnetic shape memory alloys from first-principles, *J. Magn. Magn. Mater.*, 2023, 170876.
63 S. Skaftouros, E. Ş. Kemal Özdoğan and I. Galanakis, Generalized Slater-Pauling rule for the inverse Heusler compounds, *Phys. Rev. B: Condens. Matter Mater. Phys.*, 2013, **87**(2), 024420.
64 N. Kervan and S. Kervan, Half-metallic properties of $Ti_2FeSi$ full-Heusler compound, *J. Phys. Chem. Solids*, 2011, **72**(11), 1358–1361.


© 2024 The Author(s). Published by the Royal Society of Chemistry

Open Access Article. Published on 23 February 2024. Downloaded on 2/5/2026 12:43:03 AM.
This article is licensed under a Creative Commons Attribution-NonCommercial 3.0 Unported Licence.

65 L. Offernes, P. Ravindran and A. Kjekshus, Electronic structure and chemical bonding in half-Heusler phases, *J. Alloys Compd.*, 2007, **439**(1–2), 37–54.
66 I. Galanakis, P. H. Dederichs and N. Papanikolaou, *Phys. Rev. B: Condens. Matter Mater. Phys.*, 2002, **66**(17), 174429.
67 P. Kurz, G. Bihlmayer and S. Blügel, Magnetism and electronic structure of hcp Gd and the Gd (0001) surface, *J. Phys.: Condens. Matter*, 2002, **14**(25), 6353.
68 M. A. Blanco, E. Francisco and V. Luana, GIBBS: isothermal-isobaric thermodynamics of solids from energy curves using a quasi-harmonic Debye model, *Comput. Phys. Commun.*, 2004, **158**(1), 57–72.
69 M. Flórez, J. M. Recio, E. Francisco, M. A. Blanco and A. Martín Pendás, First-principles study of the rocksalt–cesium chloride relative phase stability in alkali halides, *Phys. Rev. B: Condens. Matter Mater. Phys.*, 2002, **66**(14), 144112.
70 X.-Z. Wang, Extension of Debye's theory of specific heats of solids, *J. Phys.: Condens. Matter*, 2008, **20**(29), 295207.
71 M. M. Petit and I. Dulong, XLIV. Researches on some important points of the theory of heat, *Philos. Mag.*, 1819, **54**(258), 267–275.
72 M. Chehrouri, B. Doumi, A. Mokaddem, Y. Mogulkoc, M. Berber and A. Boudali, Investigation of structural stability, elastic properties, electronic structure and ferrimagnetic behavior of Mn2RhGe full-Heusler alloy, *J. Alloys Compd.*, 2017, **722**, 564–568.
73 J. L. Moran-Lopez, R. Rodriguez-Alba and F. Aguilera-Granja, Modeling the magnetic properties of Heusler alloys, *J. Magn. Magn. Mater.*, 1994, **131**(3), 417–426.
74 L. Wollmann, S. Chadov, J. Kübler and C. Felser, Magnetism in cubic manganese-rich Heusler compounds, *Phys. Rev. B: Condens. Matter Mater. Phys.*, 2014, **90**(21), 214420.
75 J. M. K. Al-zyadi, G. Y. Gao and K.-L. Yao, First-principles investigation of the structural and electronic properties of bulk full-Heusler alloy $Mn_2CoSn$ and its (001) surface, *J. Alloys Compd.*, 2013, **565**, 17–21.
76 J. Ma, J. He, D. Mazumdar, K. Munira, S. Keshavarz, T. Lovorn, C. Wolverton, A. W. Ghosh and W. H. Butler, Computational investigation of inverse Heusler compounds for spintronics applications, *Phys. Rev. B*, 2018, **98**(9), 094410.
77 C. Ambrosch-Draxl and J. O. Sofo, Linear optical properties of solids within the full-potential linearized augmented planewave method, *Comput. Phys. Commun.*, 2006, **175**(1), 1–14.
78 N. Kaur, R. Sharma, Y. Al-Douri, V. Srivastava and A. F. A. El-Rehim, Thermodynamic, thermoelectric and optoelectronic performances of $Co_2MB$ (M = Nb, Ta) full-heusler compounds for solar cell and UV absorber applications, *Mater. Sci. Semicond. Process.*, 2023, **165**, 107676.